ADVANCED MATERIALS
www.advmat.de

A Sulfur Heterocyclic Quinone Cathode Towards High-Rate and Long-Cycle Aqueous Zn-Organic Batteries

Qi-Qi Sun, Tao Sun, Jia-Yi Du, Kai Li, Hai-Ming Xie, Gang Huang,* and Xin-Bo Zhang**

Organic materials have attracted much attention in aqueous zinc-ion batteries (AZIBs) due to their sustainability and structure-designable, but their further development is hindered by the high solubility, poor conductivity, and low utilization of active groups, resulting in poor cycling stability, terrible rate capability, and low capacity. In order to solve these three major obstacles, a novel organic host, benzo[b]naphtho[2',3':5,6][1,4]dithiino[2,3-i]thianthrene-5,7,9,14,16,18-hexone (BNDTH), with abundant electroactive groups and stable extended π-conjugated structure is synthesized and composited with reduced graphene oxide (RGO) through a solvent exchange composition method to act as the cathode material for AZIBs. The well-designed BNDTH/RGO composite exhibits a high capacity of 296 mAh g^{-1} (nearly a full utilization of the active groups), superior rate capability of 120 mAh g^{-1}, and a long lifetime of 58 000 cycles with a capacity retention of 65% at 10 A g^{-1}. Such excellent performance can be attributed to the ingenious structural design of the active molecule, as well as the unique solvent exchange composition strategy that enables effective dispersion of excess charge on the active molecule during discharge/charge process. This work provides important insights for the rational design of organic cathode materials and has significant guidance for realizing ideal high performance in AZIBs.

1. Introduction

The burning of fossil fuels has supported the development of modern civilization, but the environmental issues caused by it have aroused great concern. At the same time, energy consumption continues to rise dramatically along with the process of modernization. Under this background, the exploitation of clean energy storage and conversion technology has been considered as a major task of human society.[1–3] In the past three decades, battery technology has profoundly changed the way of living and production today. Among all the commercialized electrochemical energy storage devices, lithium-ion batteries have attracted wide attention due to their advantages, such as higher energy density and longer cycle life. However, the limited lithium resources, toxic organic electrolyte, and potential safety hazards have hindered their further application in large-scale energy storage.[4,5] Among the energy storage systems beyond lithium-ion batteries, aqueous zinc-ion batteries (AZIBs) have aroused scientists' interest because of the high theoretical capacity (820 mAh g^{-1}), appropriate redox potential (−0.762 V vs the standard hydrogen electrode (SHE)), and high abundance of Zn anode and the nontoxicity of aqueous electrolytes.[6–8] At present, many inorganic cathode materials have been used in AZIBs, like manganese oxides, vanadium oxides, Prussian blue analogs, etc.[9–11] However, the high charge to ionic radius ratio of Zn^{2+} and the strong Coulombic interactions lead to the slow diffusion of ions in these host lattices. In addition, the repeated insertion of Zn^{2+} is easy to cause the collapse and dissolution of inorganic materials, resulting in poor electrochemical performance. Therefore, it is critical to explore suitable new host cathode materials for AZIBs.

Organic electrode materials (OEMs) have the advantages of low cost, environmentally friendly, and abundant raw material sources, which meet the requirements of humanity for sustainable development.[12,13] Meanwhile, OEMs can also find fit places in multivalent metal ion batteries because of their unique energy storage mechanism.[14,15] The storage/release of multivalent ions in OEMs is realized through reversible coordination reactions of active functional groups, and their tunable internal space can accommodate carriers with large sizes. Among the available OEMs, the application of organic carbonyl compounds as high performance cathode materials in AZIBs have

Q.-Q. Sun, H.-M. Xie
National & Local United Engineering Laboratory for Power Battery
Department of Chemistry
Northeast Normal University
Changchun, Jilin 130024, China
E-mail: xiehm136@nenu.edu.cn
Q.-Q. Sun, J.-Y. Du, K. Li, G. Huang, X.-B. Zhang
State Key Laboratory of Rare Earth Resource Utilization
Changchun Institute of Applied Chemistry
Chinese Academy of Sciences
Changchun 130022, China
E-mail: ghuang@ciac.ac.cn; xbzhang@ciac.ac.cn
T. Sun
Institute of Quantum and Sustainable Technology
School of Chemistry and Chemical Engineering
Jiangsu University
212013Zhenjiang, China
J.-Y. Du, G. Huang, X.-B. Zhang
School of Applied Chemistry and Engineering
University of Science and Technology of China
Hefei 230026, China

The ORCID identification number(s) for the author(s) of this article can be found under https://doi.org/10.1002/adma.202301088

DOI: 10.1002/adma.202301088

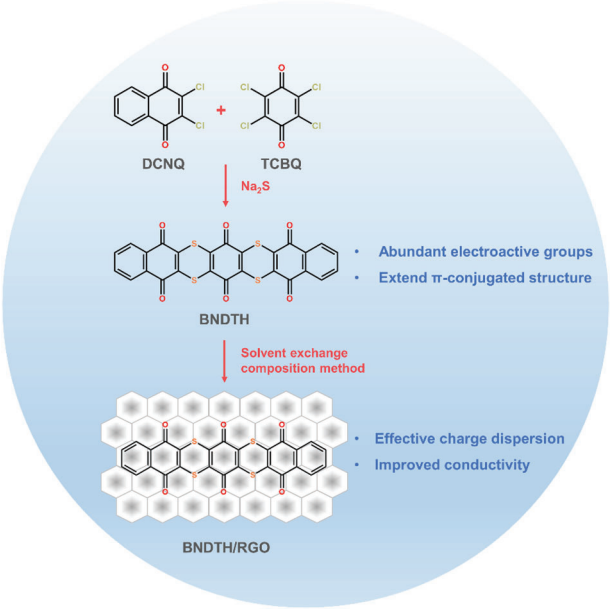

Figure 1. Schematic illustration for the synthesis of BNDTH/RGO.

been received increasing attention.[16,17] Quinones, an important class of carbonyl compounds, stand out due to their high reaction activity, large specific capacity, and exceptional electrochemical reversibility.[18–21] Ideally, the quinone molecules with lower molecular weight and abundant active groups can achieve high theoretical capacity.[22,23] Unfortunately, the practical electrochemical performance of most quinones is restricted by the low utilization of active sites for various unsolved reasons. Beyond that, just like most OEMs, the intrinsic poor conductivity and high solubility in the electrolyte are always considered as the major disadvantages of quinones, which severely restrict their potential. To address the aforementioned challenges, large amounts of carbon black and various conductive matrixes have been simply added to the electrode preparation process, but this does not solve the fundamental problems. Hence, it is important to unveil the deep-seated reasons for the low utilization of active sites and propose an effective strategy to address the relevant restrictions, thus reducing the gap between theory and practice.[24,25]

Herein, we have synthesized a sulfur heterocyclic organic quinone, Benzo[b]naphtho[2',3':5,6][1,4]dithiino[2,3-i]thianthrene-5,7,9,14,16,18-hexone (BNDTH), with six carbonyl groups and extended π-conjugated structure (**Figure 1**). On the one hand, the increase of active site number enlarges the theoretical specific capacity of BNDTH; on the other hand, the expansion of π-conjugated could enhance the intermolecular interactions, inhibiting the dissolution of BNDTH and accelerating electron transfer, and the S···S intermolecular interaction brings a further stabilization function. Despite promising, the added active functional groups of BNDTH cannot play all their roles due to its inability to take up excessive charge transfer during the discharge/charge process, while the rate capability is mainly restricted by the low conductivity. In response to these shortcomings, the BNDTH has been further designed to combine with the reduced graphene oxide (RGO) through a solvent exchange composition strategy. When the 1-Methyl-2-pyrrolidinone (NMP) solution of BNDTH and RGO is rapidly injected into ethanol, the BNDTH molecules undergo a secondary aggregation process and then precipitate on the RGO with strong π–π interaction due to the poor solvent ability of ethanol, consequently, obtaining a fully composited BNDTH/RGO. In the BNDTH/RGO, the RGO as a conductive substrate could effectively improve the composite conductivity and undertake the rapid transfer of overloaded charge on the BNDTH molecule, successfully increasing the rate capability and utilization of active groups. As expected, the resultant BNDTH/RGO composite shows superior electrochemical performance when applied as the cathode in AZIBs: a high reversible capacity (296 mAh g^{-1}, nearly a 100% utilization of the active groups), ultrastable cycling performance (65% capacity retention after 58 000 cycles at 10 A g^{-1}), and remarkable rate capability (120 mAh g^{-1} at 10 A g^{-1}). Both the experiments and theoretical calculations have clearly proved that the interaction between the RGO and BNDTH changes the reaction path and transfers the accumulated charges, which is of great significance to enable the practical performance of BNDTH to approach the theoretical values.[26,27]

2. Results and Discussion

As shown in Figure S1 (Supporting Information), the starting compound 2,3-dichloro-1,4-naphthoquinone (DCNQ) has a flat discharge/charge platform and achieves a discharge capacity of 157.5 mAh g^{-1}, corresponding to the active group utilization of 67%. A pair of redox peaks consistent with the discharge/charge profile can be found in the CV curve, which proves the one-step two-electron reaction mechanism of carbonyls.[28] Unfortunately, the DCNQ suffers severe capacity decay due to its dissolution in the aqueous electrolyte, leaving a capacity of 83 mAh g^{-1} after only 40 cycles. A visible color change of the separator due to the DCNQ dissolution can be observed in Figure S4 (Supporting Information).

To conquer the deficiencies of DCNQ, BNDTH with enhanced stability and theoretical specific capacity (296 mAh g^{-1}) was synthesized through a two-step reaction.[29] As shown in Figure S2a (Supporting Information), the characteristic peaks of the Fourier transform infrared (FTIR) spectra at 1662 and 1651 cm^{-1} can be attributed to the stretching vibration of the carbonyl groups. The absorption peaks at 1585 and 1536 cm^{-1} correspond to the stretching vibration of C=C bonds in the aromatic ring. The peaks at 1284, 1146, and 791 cm^{-1} can be ascribed to the C–H bending vibration in the aromatic rings. The peak at 705 cm^{-1} is allocated to the stretching vibration of C–S bonds. All these indicate the successful synthesis and high purity of the obtained BNDTH. The ^{1}H-NMR spectrum in Figure S2b (Supporting Information) with the chemical shifts of 7.88 and 8.00 ppm corresponding to the two types of H and the symmetric structure of BNDTH further confirms this. The solid-state ^{13}C NMR spectrum also verifies the purity of the obtained BNDTH (Figure S2c, Supporting Information). The X-ray diffraction (XRD) pattern shows that the BNDTH has certain crystallinity (Figure S2d, Supporting Information).

The redox behavior of BNDTH was investigated in AZIBs. It can be observed from **Figure 2**a that the BNDTH displays one pair of redox peaks at 0.73 V/1.01 V versus Zn^{2+}/Zn. Correspondingly, a pair of respective flat plateaus can be clearly

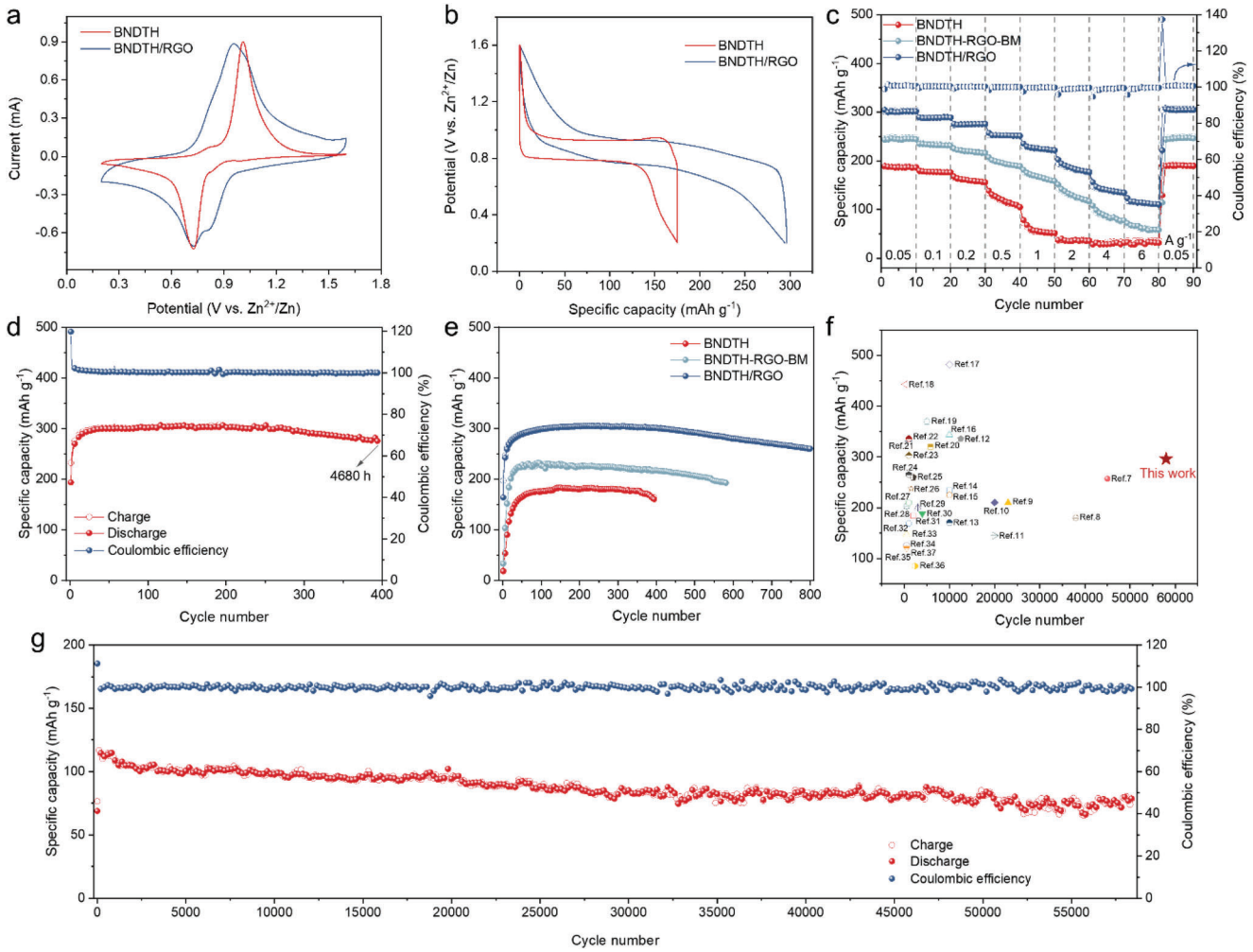

Figure 2. a) CV curves of BNDTH and BNDTH/RGO at a scan rate of 0.5 mV s^{-1}. b) Discharge/charge curves of BNDTH and BNDTH/RGO at 0.05 A g^{-1}. c) Rate performance of BNDTH, BNDTH-RGO-BM, and BNDTH/RGO. d,e) Cycling performance of (d) BNDTH/RGO at 0.05 A g^{-1}, (e) BNDTH, BNDTH-RGO-BM, and BNDTH/RGO at 0.1 A g^{-1}. f) Capacity and cycle life comparison with reported typical cathode materials in AZIBs (the numbers refer to references in Supporting Information). g) Cycling performance of BNDTH/RGO at 10 A g^{-1}.

distinguished from the discharge/charge profile, exhibiting high reversibility with a capacity of 174.7 mAh g^{-1} (Figure 2b). Compared with DCNQ, BNDTH has a larger π-conjugated structure, and the presence of S atoms makes the interaction between the molecules stronger, so both BNDTH and the corresponding discharge product can stably exist in the aqueous solution.[30] As a result, the BNDTH exhibits excellent stability in electrochemical tests, and no active material dissolves on the separator even after 200 cycles at 50 mA g^{-1} (Figures S3 and S4, Supporting Information). Despite the high cycling stability, the BNDTH obviously fails to achieve the expected performance due to its poor utilization of active groups (59%) and low electrical conductivity (Figure S3, Supporting Information). In order to address these two problems simultaneously, a facile strategy was developed to fabricate a BNDTH/RGO composite by a solvent exchange composition method. With the selection of appropriate solvents (NMP and ethanol here), the BNDTH molecules could undergo a secondary aggregation process and then realize the homogeneous precipitation of BNDTH on the RGO, getting a BNDTH/RGO composite with strong π–π interaction. The morphology of the prepared BNDTH/RGO was characterized by scanning electron microscopy (SEM, Figure S5, Supporting Information). Compared with BNDTH, the active BNDTH bulk in the composite is well wrapped within the RGO sheets. The content of BNDTH in BNDTH/RGO was determined to be about 66.60% by thermogravimetric (TG) and elemental analyses (Figure S6 and Table S1, Supporting Information). Owing to the synergistic effects between the BNDTH with robust multi-active sites structure and RGO with excellent conductivity, the three major challenges of OEMs (strong solubility, poor conductivity, and low utilization of active functional groups) could be solved at the same time.[31,32] As shown in Figure 2a, the BNDTH/RGO exhibits two pairs of redox peaks at 0.74 V/0.81 V and 0.84 V/0.98 V. The decrease in the potential of the oxidation peak indicates a reduced energy barrier to initiate the electrochemical reaction. This is further confirmed by the electrochemical impedance spectroscopy (EIS) results obtained on BNDTH and BNDTH/RGO coin cells (Figure S7, Supporting Information), in which the

charge transfer resistance of BNDTH/RGO is greatly reduced. Moreover, the area of the CV curve for BNDTH/RGO increases with the appearance of a new pair of redox peaks. This can be further proved by the differential capacity curves (Figure S8, Supporting Information), in which the presence of new peaks means that the original recessive active groups have begun to work, indicating a change in the reaction path.[33] Meanwhile, benefiting from the excess charge flowing from BNDTH to RGO, the CV curves reveal that the original weak peak in the shoulder of BNDTH also begins to contribute capacity, improving the utilization of active groups. And BNDTH/RGO delivers a reversible capacity of 296 mAh g^{-1} (based on the mass of BNDTH) in Figure 2b. The above results show that the full utilization of active groups depends on the effective transfer of charge.

The rate performance of BNDTH/RGO||Zn batteries was also evaluated. As indicated in Figure 2c, the BNDTH/RGO shows stable reversible capacities of 289, 274, 252, 222, 176, 135, and 115 mAh g^{-1} at current densities of 0.1, 0.2, 0.5, 1, 2, 4, and 6 A g^{-1}, respectively. When the current density decreases from 6 to 0.05 A g^{-1}, the specific discharge capacity is able to recover to the initial value, revealing the superior rate capability of BNDTH/RGO. Furthermore, the BNDTH/RGO||Zn cell sustains a capacity retention of 95% and delivers a capacity of 283 mAh g^{-1} after 4680 h cycles at 0.05 A g^{-1} (Figure 2d). It is noted that a considerable capacity of 110 mA h g^{-1} could still be obtained even under an extremely high rate of 10 A g^{-1} (Figure 2g). The corresponding charge time is as short as 43 s, exhibiting ultrafast discharge/charge ability. Under such a test condition, the battery could maintain a capacity retention of approximately 65% over 58 000 cycles, confirming the excellent cycling stability of BNDTH/RGO. To the best of our knowledge, such a long cycling lifetime has not been reported before (Figure 2f). The cycling performance of BNDTH/RGO at different current densities was also tested and shown in Figure S9 (Supporting Information), in which all possess high stability with coulombic efficiency ≈100%. After disassembling the failed battery, we can see the serious corrosion of the zinc anode, which is the main reason for limiting the continued operation of the battery. In the Zn-organic aqueous batteries, the zinc anode would experience hydrogen evolution, corrosion, passivation, and dendrite. When replacing new zinc foil anode, the BNDTH/RGO||Zn cell can run normally again with high cycling stability (Figures S10 and S11, Supporting Information), indicating the robustness of the designed BNDTH/RGO. This can be ascribed to the extended π-conjugated structure of BNDTH and the strong π–π intermolecular interactions with RGO. In addition, the BNDTH/RGO has consistent FTIR spectra and XRD diffraction peaks at different electrochemical states, which is an important reason for its extraordinary cycling stability (Figures S12 and S13, Supporting Information).[34]

The capacity increase of the BNDTH/RGO||Zn cell at the beginning of cycling (Figure 2) can be attributed to the gradual activation of the BNDTH/RGO electrode due to its initial insufficient contact with the electrolyte.[35,36] The gradual enlargement of the area of CV curves during cycling also demonstrates the increase of specific capacity (Figure S14a, Supporting Information). Then, the activation process was investigated by EIS measurement. As shown in Figure S14b (Supporting Information), the overall resistance decreases step by step during the activation process. These results indicate that the utilization ratio of the active groups of BNDTH/RGO undergoes an activation process at the early stage of cycling.

To demonstrate the performance improvement of BNDTH/RGO is not just by the electrical conductivity enhancement enabled by RGO, a control sample with 30 wt.% BNDTH and 60 wt.% conductive Super P was prepared (denoted as BNDTH361) and conducted the electrochemical tests under the same conditions. Obviously, the elevation of the active group utilization and rate capability of BNDTH361 is limited (Figure S15, Supporting Information). This suggests that simply increasing the electrical conductivity of the electrode does not address the underlying problems that limit the full performance liberation of BNDTH. As shown in Figure S16 (Supporting Information), the capacity provided by pure RGO is only 30 mAh g^{-1}, signifying that most of the capacity delivered by BNDTH/RGO is from BNDTH. In addition, for a sufficient comparison, the traditional ball milling method was used to fabricate BNDTH and RGO hybrid (marked as BNDTH-RGO-BM), which exhibited improved utilization of active groups (81%) and optimized rate and cycling performance synchronously (Figure 2c,e). However, the overall performance of BNDTH-RGO-BM is still much inferior to that of BNDTH/RGO due to the simple ball milling cannot adequately combine BNDTH and RGO. Unlike the ball milling process, the solvent exchange composition method makes the active molecule undergo the process of reaggregation, which is conducive to its close and firm contact with RGO.[37,38] As a result, it is beneficial to the rapid electron transfer between BNDTH and RGO and enhances the stability of the active molecule.

The redox kinetics of BNDTH/RGO were studied by CV curves at different scan rates (**Figure 3**a). As the scan rate increases from 0.1 to 2 mV s^{-1}, the CV curves maintain a similar shape, and the polarization just increases slightly. The relationship between the redox peak current i and the potential sweep rate v obeys the power-law equation of $i = av^b$, where a and b are adjustable parameters. The b-value close to 0.5 indicates the diffusion-controlled process, and 1.0 indicates the capacitance-dominated process.[39] As shown in Figure 3b, the calculated b-value approaches 1.0 for both the anodic peaks (0.882, 0.723) and cathodic peaks (0.802, 0.741), implying that the redox reactions of BNDTH/RGO are dominated by the capacitive processes. To further investigate the contribution percentage of surface-controlled capacity at various scan rates, the specific capacity was divided into the surface-controlled capacity (k_1v) and diffusion-controlled capacity ($k_2v^{1/2}$), written as: $i = k_1v + k_2v^{1/2}$. Obviously, as the acceleration of scan rate from 0.1 to 2 mV s^{-1}, the proportion of capacity contributed by the capacitive process increases from 55.29% to 85.02% (Figure 3c,d; Figure S17, Supporting Information). This certifies that the capacitive process plays a leading role at high rates, which is conducive to achieving better rate capability. On the contrary, the b values for the oxidation and reduction peaks of BNDTH are close to 0.5 (Figure S18, Supporting Information), and consequently, the BNDTH possesses a diffusion-controlled electrochemical process, consistent with its flat charge/discharge curves and poor rate performance.

In order to further understand the electrochemical mechanism of BNDTH/RGO, a series of ex-situ structural characterizations was carried out. **Figure 4**a shows the EDS mapping

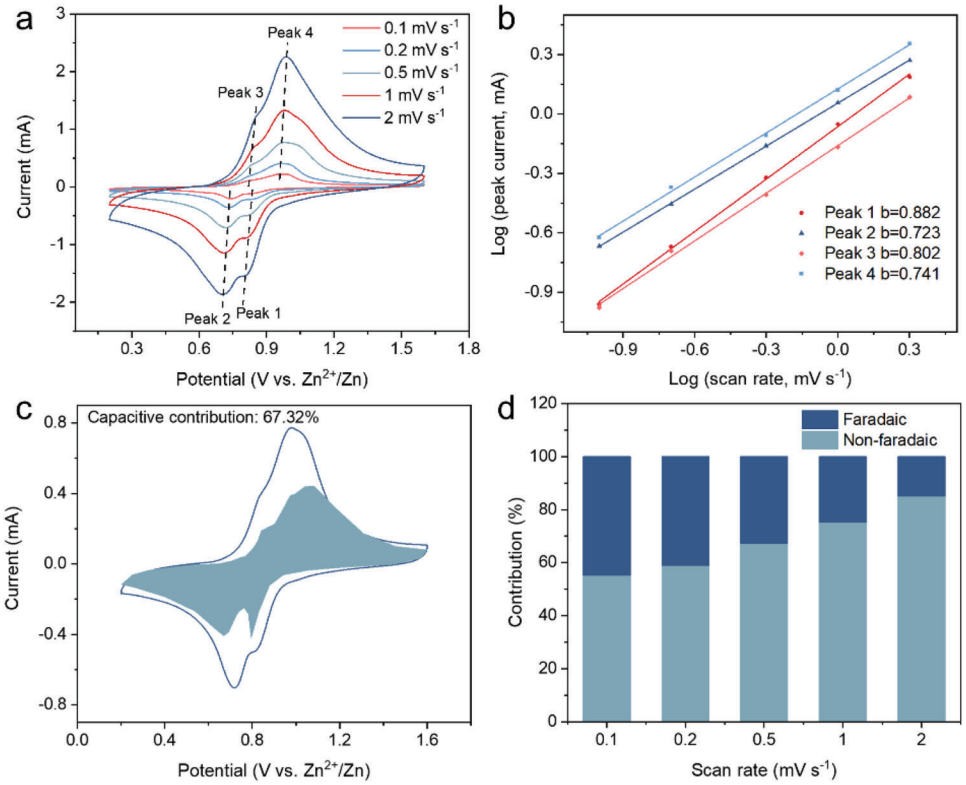

Figure 3. a) CV curves of BNDTH/RGO at various scan rates. b) Power law dependence of measured current on scan rate at corresponding peak potentials. c) Capacitive contribution at 0.5 mV s^{-1}. The red area shows the contribution from the capacitive charge storage. d) Contribution ratios of the capacitive charge storage at different scan rates.

of the pristine, fully discharged, and fully recharged BNDTH/RGO. Comparing the distributions of C, O, S, and Zn elements, a reversible process of Zn^{2+} insertion/extraction on the BNDTH/RGO cathode could be obviously demonstrated during a discharge/charge cycle. FTIR spectroscopy was subsequently performed to reveal the structural evolution of BNDTH/RGO (Figure 4b). The characteristic peaks at 1650 cm^{-1} for the stretching vibration of carbonyl group are gradually weakened during the discharge process, implying the continuous coordination of Zn^{2+} with carbonyl groups. In the succeeding charge process, these peaks gradually strengthen and eventually return to their original state, demonstrating the high reversibility of Zn^{2+} storage in BNDTH/RGO electrode. Furthermore, X-ray photoelectron spectroscopic (XPS) analysis was performed to check the surface evolution of BNDTH/RGO. In order to obtain more accurate characterization, the sample electrodes have undergone four complete cycles at 0.02 A g^{-1}. In the fully discharged state, the strong peaks corresponding to Zn 2p are clearly observed (Figure 4c), proving the insertion of Zn^{2+}, while the weak Zn 2p peaks in the charged state at 1.6 V imply the reversible removal of Zn^{2+}. In addition, the aprotic acetonitrile (AN) was used as the solvent to prepare 1 M $Zn(CF_3SO_3)_2$/AN electrolyte for electrochemical testing, in which the BNDTH/RGO has the same specific capacity as in the aqueous electrolyte (Figure S19a, Supporting Information).[40,41] Although the cycling stability of BNDT/RGO is affected by the strong polarity of acetonitrile, this result is sufficient to demonstrate that the electrochemical activity of BNDTH/RGO is toward Zn^{2+}.[42] This can be further confirmed by the low capacity of BNDTH/RGO when using the 1 M H_2SO_4 as the electrolyte, and a specific capacity of only 45 mAh g^{-1} can be delivered even at a high H^+ concentration (Figure S19, Supporting Information).

Theoretical calculation was then conducted to further deduce the energy storage mechanism of BNDTH/RGO. It can be seen from the electrostatic potential (ESP) mapping that the carbonyl groups and S heteroatoms together constitute the active region to coordinate with Zn^{2+} (**Figure 5**a). In order to better understand the interaction between BNDTH and RGO, the differential charge density diagram was obtained by VASP (Figure 5b; Figure S20, Supporting Information). It is clear that the electrons on RGO are obviously concentrated in the BNDTH region, indicating there is a strong π–π interaction between the BNDTH and RGO. It is also shown that the BNDTH and RGO have a strong adsorption energy of −2.23 eV and the ability of charge transfer between them.[43] The highest occupied molecular orbital (HOMO) map gives the positions of the valence shell electrons and provides qualitative information on the electronic structure of the molecule. Whenever the carbonyl groups in BNDTH are reduced, the enolization would occur to delocalize the negative charge, and the adjacent carbonyl groups contribute to the formation of stable enolate anions through electron withdrawing and conjugation capabilities. In Figure 5c and Figure S21 (Supporting Information), efficient conjugation between the carbonyl groups and the aromatic ring could be observed in each of the reduced states of BNDTH, resulting in excellent stabilization.

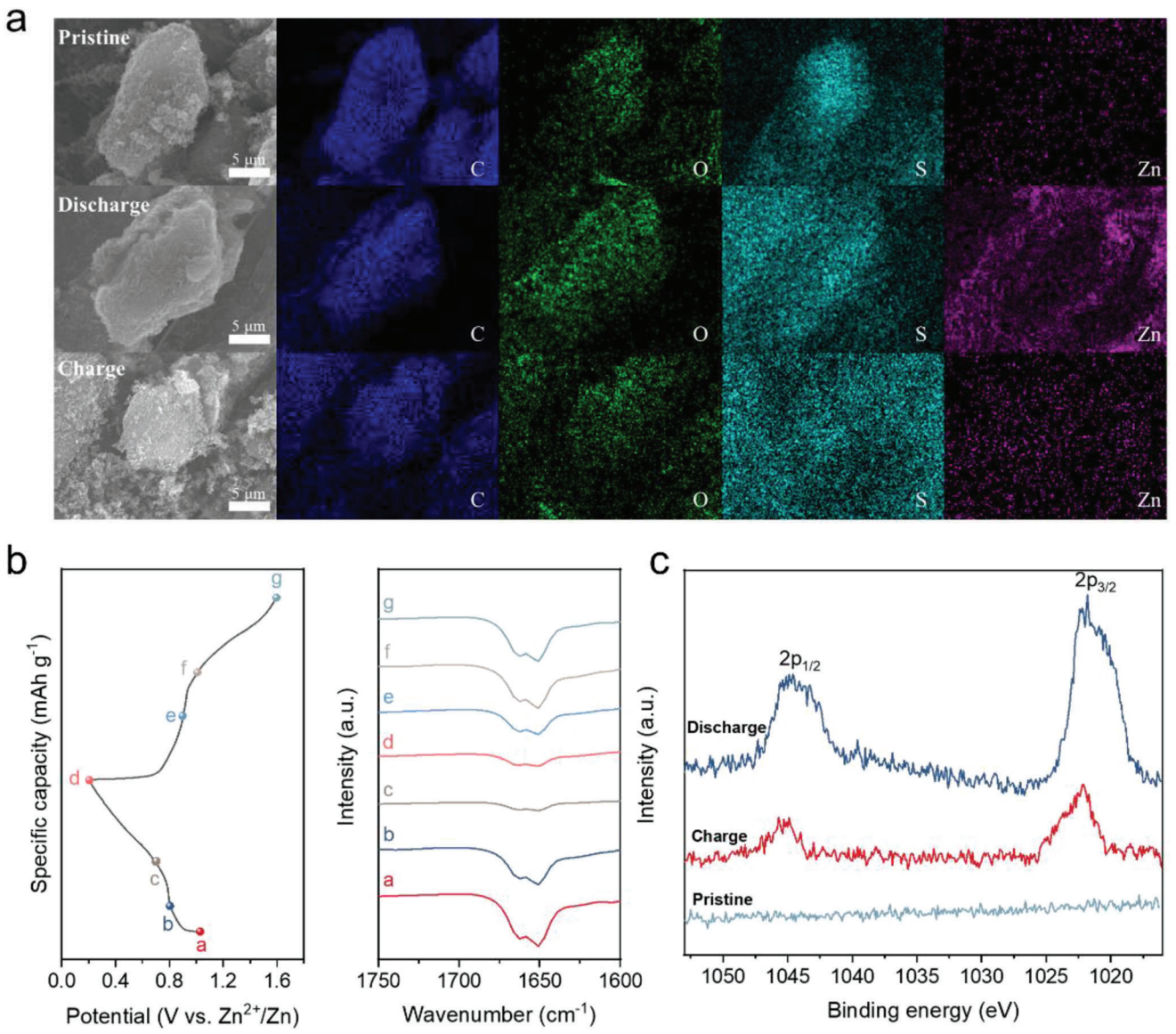

Figure 4. a) SEM images and SEM-EDS mapping of C, O, S, and Zn elemental distributions of BNDTH/RGO electrodes at (i) pristine, (ii) fully discharged (0.2 V), and (iii) fully recharged (1.6 V) states. b) Ex situ FTIR spectra of BNDTH/RGO electrode at different discharge/charge states. c) Ex situ XPS spectra of Zn 2p region at fully discharged (0.2 V) and fully recharged (1.6 V) states.

Even when the six-electron reduction occurs, the HOMO of BNDTH can still remain within the structure without extending out of the molecule, which means that the backbone of the molecule can fully support such a large number of negative charges. However, the realization of six-electron reduction of BNDTH also needs the assistance of a conductive substrate. From the HOMO plots of BNDTH/RGO we can see, the BNDTH and RGO share negative charges in various reduced states (Figure S22, Supporting Information). The enhanced charge delocalization could facilitate the electron to inject into the organic host. The comparison of the HOMO/LUMO energy gaps between BNDTH and BNDTH/RGO in various reduction states shows that the BNDTH/RGO always has significantly decreased gaps (Figure 5d; Figures S21 and S22, Supporting Information). Based on molecular orbital theory, a narrow energy band gap (E_{gap}) represents efficient electronic conduction at a lower energy barrier. Therefore, the dispersion of excess charge by RGO could enable the six-electron reduction of BNDTH to proceed smoothly, and accordingly improves its utilization rate of active groups close to 100%.

Considering the excellent electrochemical performance for the coin-type batteries, a belt-shaped and flexible aqueous cell was also assembled to demonstrate the practical potential application of BNDTH/RGO. As expected, the belt-shaped BNDTH/RGO||Zn cell also delivers a high specific capacity of 291 mAh g^{-1} at 0.05 A g^{-1}, and a long cycle life of 1600 cycles with a capacity retention of 76% at 0.5 A g^{-1} (Figure S23, Supporting Information), well reproducing the performance that was achieved with coin batteries. To demonstrate the viability of belt-shaped BNDTH/RGO||Zn cell in flexible electronic devices,

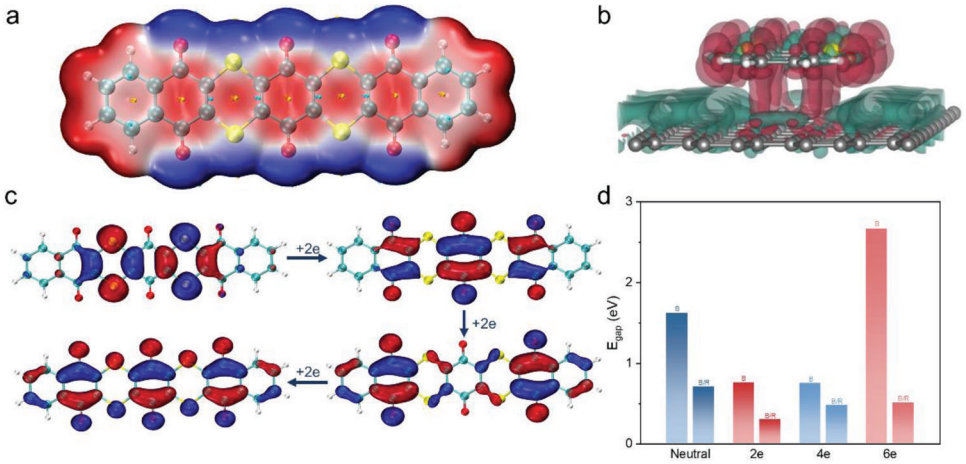

Figure 5. a) The ESP-mapped molecular van der Waals surface of BNDTH. b) The difference charge density map of BNDTH/RGO. c) HOMO plots of selected molecules/anions with different extents of reduction of BNDTH. d) HOMO/LUMO energy gaps (E_{gap}) of BNDTH and BNDTH/RGO.

a series of flexibility tests were conducted by bending the cell at different angles. As shown in Figure S23b (Supporting Information), when folded to 45, 90, 135, and 180°, the belt-shaped cell is almost with no capacity loss, revealing its good flexibility and robust mechanical stability, and thus demonstrating its potential in wearable applications.[44]

3. Conclusion

In summary, we have synthesized a structurally stable BNDTH with multi-active sites through a rational molecular design and further efficiently compounds it with RGO through a solvent exchange composition strategy. The obtained BNDTH/RGO successfully achieves a full utilization of the active groups and displays excellent rate performance (capacity retention of ≈65% at 10 A g^{-1}) and long-term cycling stability (more than 58 000 cycles at 10 A g^{-1}). Based on the analysis of reaction kinetics and energy storage mechanism, it can be deduced that the extraordinary electrochemical performance is derived from the stable and close contact between BNDTH and RGO, wherein the effective dispersion of excess charge from BNDTH to RGO plays the key role in improving the utilization of active groups. This study indicates that a reasonably designed organic carbonyl molecule can be used as high-performance electrode material for multivalent metal ion storage. Our research provides some insights into the full utilization of organic cathode materials and is expected to serve as a reference for molecular design in the future.

Supporting Information

Supporting Information is available from the Wiley Online Library or from the author.

Acknowledgements

Q.-Q.S., T.S., and J.-Y.D. contributed equally to this work. This work was financially supported by the National Key R&D Program of China (Grant 2022YFB2402200), the National Natural Science Foundation of China (Grant 52271140, 52171194), Changchun Science and Technology Development Plan Funding Project (Grant 21ZY06), and Youth Innovation Promotion Association CAS (Grant 2021223).

Conflict of Interest

The authors declare no conflict of interest.

Data Availability Statement

The data that support the findings of this study are available from the corresponding author upon reasonable request.

Keywords

carbonyl compound materials, organic electrodes, Zn-ion batteries, Zn-organic batteries

Received: February 3, 2023
Revised: March 30, 2023
Published online:

[1] S. Chu, A. Majumdar, *Nature* **2012**, *488*, 294.
[2] D. Larcher, J.-M. Tarascon, *Nat. Chem.* **2015**, *7*, 19.
[3] Z. Yang, J. Zhang, M. C. W. Kintner-Meyer, X. Lu, D. Choi, J. P. Lemmon, J. Liu, *Chem. Rev.* **2011**, *111*, 3577.
[4] P. K. Nayak, L. Yang, W. Brehm, P. Adelhelm, *Angew. Chem., Int. Ed.* **2018**, *57*, 102.
[5] X.-B. Cheng, R. Zhang, C.-Z. Zhao, Q. Zhang, *Chem. Rev.* **2017**, *117*, 10403.
[6] B. Tang, L. Shan, S. Liang, J. Zhou, *Energy Environ. Sci.* **2019**, *12*, 3288.
[7] X. Jia, C. Liu, Z. G. Neale, J. Yang, G. Cao, *Chem. Rev.* **2020**, *120*, 7795.
[8] K. W. Nam, S. S. Park, R. Dos Reis, V. P. Dravid, H. Kim, C. A. Mirkin, J. F. Stoddart, *Nat. Commun.* **2019**, *10*, 4948.
[9] F. Mo, G. Liang, Q. Meng, Z. Liu, H. Li, J. Fan, C. Zhi, *Energy Environ. Sci.* **2019**, *12*, 706.
[10] G. Du, H. Pang, *Energy Storage Mater.* **2021**, *36*, 387.
[11] N. Zhang, F. Cheng, J. Liu, L. Wang, X. Long, X. Liu, F. Li, J. Chen, *Nat. Commun.* **2017**, *8*, 405.
[12] Z. Luo, L. Liu, J. Ning, K. Lei, Y. Lu, F. Li, J. Chen, *Angew. Chem., Int. Ed.* **2018**, *57*, 9443.
[13] R. Emanuelsson, M. Sterby, M. Stromme, M. Sjodin, *J. Am. Chem. Soc.* **2017**, *139*, 4828.

[14] K. Qin, J. Huang, K. Holguin, C. Luo, *Energy Environ. Sci.* **2020**, *13*, 3950.
[15] S. Wang, S. Huang, M. Yao, Y. Zhang, Z. Niu, *Angew. Chem., Int. Ed.* **2020**, *59*, 11800.
[16] F. Wan, L. Zhang, X. Wang, S. Bi, Z. Niu, J. Chen, *Adv. Funct. Mater.* **2018**, *28*, 1804975.
[17] Y. Wang, C. Wang, Z. Ni, Y. Gu, B. Wang, Z. Guo, Z. Wang, D. Bin, J. Ma, Y. Wang, *Adv. Mater.* **2020**, *32*, 2000338.
[18] D. Kundu, P. Oberholzer, C. Glaros, A. Bouzid, E. Tervoort, A. Pasquarello, M. Niederberger, *Chem. Mater.* **2018**, *30*, 3874.
[19] Y. Liang, Y. Jing, S. Gheytani, K.-Y. Lee, P. Liu, A. Facchetti, Y. Yao, *Nat. Mater.* **2017**, *16*, 841.
[20] T. Sun, W. Zhang, Q. Nian, Z. Tao, *Nano-Micro Lett.* **2023**, *15*, 36.
[21] Y. Zhang, C. Zhao, Z. Li, Y. Wang, L. Yan, J. Ma, Y. Wang, *Energy Storage Mater.* **2022**, *52*, 386.
[22] J. Xie, F. Yu, J. Zhao, W. Guo, H.-L. Zhang, G. Cui, Q. Zhang, *Energy Storage Mater.* **2020**, *33*, 283.
[23] Z. Guo, Y. Ma, X. Dong, J. Huang, Y. Wang, Y. Xia, *Angew. Chem., Int. Ed.* **2018**, *57*, 11737.
[24] D. J. Kim, D.-J. Yoo, M. T. Otley, A. Prokofjevs, C. Pezzato, M. Owczarek, S. J. Lee, J. W. Choi, J. F. Stoddart, *Nat. Energy* **2019**, *4*, 51.
[25] M. Yu, R. Dong, X. Feng, *J. Am. Chem. Soc.* **2020**, *142*, 12903.
[26] Y. Zhao, Y. Wang, Z. Zhao, J. Zhao, T. Xin, N. Wang, J. Liu, *Energy Storage Mater.* **2020**, *28*, 64.
[27] N. Liu, X. Wu, Y. Zhang, Y. Yin, C. Sun, Y. Mao, L. Fan, N. Zhang, *Adv. Sci.* **2020**, *7*, 2000146.
[28] X. Wu, S. Jin, Z. Zhang, L. Jiang, L. Mu, Y.-S. Hu, H. Li, X. Chen, M. Armand, L. Chen, X. Huang, *Sci. Adv.* **2015**, *1*, e1500330.
[29] Z. Cai, J. Gao, B. Xiang, *Chin. J. Synth. Chem.* **2007**, *15*, 16.
[30] J. Xie, Z. Wang, Z. J. Xu, Q. Zhang, *Adv. Energy Mater.* **2018**, *8*, 1703509.
[31] Q. Zhao, Y. Lu, J. Chen, *Adv. Energy Mater.* **2017**, *7*, 1601792.
[32] Z. Zhu, J. Chen, *J. Electrochem. Soc.* **2015**, *162*, A2393.
[33] Z. Song, T. Xu, M. L. Gordin, Y.-B. Jiang, I.-T. Bae, Q. Xiao, H. Zhan, J. Liu, D. Wang, *Nano Lett.* **2012**, *12*, 2205.
[34] X. Wang, C. Bommier, Z. Jian, Z. Li, R. S. Chandrabose, I. A. Rodríguez-Pérez, P. A. Greaney, X. Ji, *Angew. Chem., Int. Ed.* **2017**, *56*, 2909.
[35] J. Wu, X. Rui, G. Long, W. Chen, Q. Yan, Q. Zhang, *Angew. Chem., Int. Ed.* **2015**, *54*, 7354.
[36] T. Sun, Z.-J. Li, X. Yang, S. Wang, Y.-H. Zhu, X.-B. Zhang, *CCS Chem.* **2019**, *1*, 365.
[37] Y. Liang, P. Zhang, S. Yang, Z. Tao, J. Chen, *Adv. Energy Mater.* **2013**, *3*, 600.
[38] K. Zhang, C. Guo, Q. Zhao, Z. Niu, J. Chen, *Adv. Sci.* **2015**, *2*, 1500018.
[39] Z. Ye, S. Xie, Z. Cao, L. Wang, D. Xu, H. Zhang, J. Matz, P. Dong, H. Fang, J. Shen, M. Ye, *Energy Storage Mater.* **2021**, *37*, 378.
[40] W. Kaveevivitchai, A. Manthiram, *J. Mater. Chem. A* **2016**, *4*, 18737.
[41] D. Kundu, S. Hosseini Vajargah, L. Wan, B. Adams, D. Prendergast, L. F. Nazar, *Energy Environ. Sci.* **2018**, *11*, 881.
[42] Y. Zhang, Y. Liang, H. Dong, X. Wang, Y. Yao, *J. Electrochem. Soc.* **2020**, *167*, 070558.
[43] L. Liu, L. Miao, L. Li, F. Li, Y. Lu, Z. Shang, J. Chen, *J. Phys. Chem. Lett.* **2018**, *9*, 3573.
[44] H. Li, C. Han, Y. Huang, Y. Huang, M. Zhu, Z. Pei, Q. Xue, Z. Wang, Z. Liu, Z. Tang, Y. Wang, F. Kang, B. Li, C. Zhi, *Energy Environ. Sci.* **2018**, *11*, 941.